40th AIAA/ASME/SAE/ASEE Joint Propulsion Conference and Exhibit
July 11-14, 2004 Fort Lauderdale, Florida

AIAA-2004-3928

Design of the Secondary Flow System for a Co-Flow Jet Cascade

Craig Paxton [*] and Ge-Cheng Zha[†]
Dept. of Mechanical Engineering
University of Miami
Coral Gables, FL 33124
Contact: zha@apollo.eng.miami.edu

David Car [‡]
AFRL/PRTF
1950 Fifth St. Bldg 18
WPAFB, OH 45433
Contact: david.car@wpafb.af.mil

This paper uses 3D CFD simulation to design the co-flow jet cascade secondary flow system. The CFD simulation located an area of massive separation from the suction side of the blade. This separation appears to be due to the end wall boundary layer on the top wall since the injection and suction jets are significantly less energetic near the top wall. It is mainly caused by the non-uniformity of the injection jet in the spanwise direction across the jet opening. Several internal duct designs were conducted with the best version being a 9-port injection duct, which has a more uniform jet in streamwise direction and provides higher mass flow rate near the tunnel walls in an attempt to reduce wind tunnel wall affects. This design provides a flow which stays attached to the surface of the blade for nearly the entire span; the end wall effects still cause a minor separation in a small region near the top wall. The co-flow jet cascade designed allows for a diffusion factor of 0.74 at an inlet Mach of 0.3.

Nomenclature

A^*	=	critical area
C_μ	=	jet momentum coefficient
DF	=	diffusion factor
$\dot{m}^*$	=	critical mass flow rate
M	=	Mach number
P_0	=	total pressure
S	=	blade area
T_0	=	total temperature
U_∞	=	freestream velocity
V_1	=	velocity magnitude at blade inlet
V_2	=	velocity magnitude at blade outlet
$V_{\theta 1}$	=	tangential velocity magnitude at blade inlet
$V_{\theta 2}$	=	tangential velocity magnitude at blade outlet
ρ_∞	=	freestream density
σ	=	solidity

[*] Graduate Student, Mechanical & Aerospace Engineering, University of Miami, AIAA student member.
[†] Associate Professor, Mechanical & Aerospace Engineering, University of Miami, AIAA member.
[‡] Aerospace Engineer, AFRL , AIAA member.

I. Introduction

TO maintain the US Air Force's superiority, revolutionary technology advancement should be pursued to dramatically reduce the weight of aircraft and space launch vehicles, significantly increase their mission payload and maneuverability. Commercial aircraft and space launch vehicles will also benefit from this same technology except that the maneuverability is not a serious concern.

In aircraft and space launch vehicle propulsion systems, there are some important components whose functions are to diffuse the flow and increase the pressure. These components include fan/compressor, inlets, combustor diffuser, space launch vehicle engine turbopumps, etc. The high lift wings also work with high diffusion. To reduce the weight of these components, the number of stages of the fan/compressors and turbopumps, or the length of the inlets, diffusers and wings, must be reduced. This usually will exacerbate the already very severe adverse pressure gradient, which may result in the aerodynamic stall of those components. Hence studying the diffusion enhancement mechanism is crucial to achieve the design of high performance aircraft and space launch vehicles.

The current technologies to achieve high diffusion aircraft engine compressor designs include forward swept rotors[1,2], bowed stators[3], tandem blades[4,5], casing treatment[6,7,8], etc. All these technologies mainly rely on the aerodynamic configuration alone. In other words, they do not make use of external device or control to improve performance. The variable stators and compressor bleed do use external control systems. However, they are only used in the transient stage and are not used to improve the performance at design points. The above technologies have significantly improved the compressor loading, efficiency and stall margin. However, it may be difficult to break the limit if we only go along the conventional route. For example, virtually no compressors can achieve a diffusion factor greater than 0.7 for their blades at design points and still maintain a stall margin.

To achieve higher diffusion in compressor blades, flow control technologies can play a very important role. For external aerodynamic airfoils, many efforts have been done to enhance lift and suppress separation[9,10], such as moving walls[11,12], circulation control[13,14,15,16,17,18], multi-element airfoils[19,20], pulsed jet separation control[21,22,23], etc. However, most of these methods are either not effective or not applicable to enhance internal flow diffusion.

To enhance diffusion using flow control for compressors, there are generally two types of methods. One is in the rotor tip region such as tip injection to improve stall margin[6,24,25,26,27,28,29,30]. The other is on the blade surface, such as the aspirated blades[31], to improve the diffusion limit and efficiency. The aspirated blade designed at MIT has achieved single stage pressure ratio of 3.5 with diffusion factor slightly over 0.7[32,33,34,35]. The aspirated blade concept is to suck away the boundary layer to avoid the flow separation and therefore increase flow turning. This is somewhat like an inviscid flow with no boundary layer. However, since the flow deviation at the compressor blade exit is mostly an inviscid phenomenon[36] this may mean that the aspirated blades can not go too far beyond the conventional loading limit. The disadvantage of the aspirated blade concept is that it dumps away the sucked flow, which is a penalty to the overall cycle efficiency.

Copenhaver et al. used an ejector pump to control the suction surface boundary layer to increase the turning and reduce the loss and blockage[37]. Both suction and blowing is used with the ejector pump. The performance of the cascade is improved. The ejector pump technique sucks a small amount of flow and injects more into the flow. A part of the flow is recycled. Unlike the aspirated blades which reduce the core mass flow, the ejector pump technique adds more flow to the core.

In the summer of 2002, the joint research team from University of Miami(UM) and AFRL studied a new flow control concept: using a co-flow wall jet to enhance the compressor cascade diffusion[38]. The research was based on 2D CFD simulations using RANS model. A very large diffusion factor, 0.965, was achieved by the CFD simulation with a certain stall margin. The diffusion factor reaches the limit of the geometry and is far greater than the current upper limit of 0.65. If the CFD results are proved to be true by experiments, the diffusion factor will be also much larger than that achieved by the aspirated blade designed at MIT[32,33,34,35]. Conceptually, using these high diffusion blades can reduce a current 6-stage compressor to a 2-stage compressor[38]. This would be a tremendous weight reduction.

The co-flow jet cascade is to inject a high energy jet along the blade suction surface in the same direction of the main flow. The jet is injected near the leading edge and the same amount of mass flow is sucked away near the trailing edge. The jet hence can be recirculated to avoid reducing or increasing the core mass flow. The turbulent shear layer between the cascade core flow and the jet causes a strong turbulence diffusion and mixing, which enhance the lateral transport of energy and allow the core flow to overcome the severe adverse pressure gradient and turn with the jet. The flow can then achieve very large diffusion due to the large turning.

The co-flow jet may be considered as an enhanced Coanda flow with blowing and suction. The conventional natural Coanda flow only has blowing. It is known that the natural Coanda flow will follow a curved wall to a certain extent and then separate from the wall when an adverse pressure gradient is built up[39]. The suction used in

this new flow control technique will hence enhance the Coanda flow so that it stays attached even when there is extremely large pressure gradient. The same concept has recently been applied to augment airfoil lift[40].

The co-flow jet cascade has two advantages: 1) it does not change the mass flow of the compressor core flow. Unlike the external aerodynamics such as a wing, the engine design is based on the constant mass flow for stage matching. Keeping the engine core mass flow constant is also very desirable to avoid harming the cycle efficiency; 2) Sucking and blowing the same amount of mass flow also makes it possible to recirculate the jet flow. In order to create the jet, there must be a flow source for the jet no matter the flow control scheme has blowing only or both blowing and suction. In other words, the jet flow must be sucked from somewhere, be energized and then blown into the core flow. From energy expenditure point of view, it is a more efficient way to suck the jet itself than sucking the free stream flow. The jet has higher energy state than the free stream flow even near the trailing edge. Hence less work needs to be done to energize the flow and the overall cycle efficiency can be higher.

To prove the co-flow jet cascade concept experimentally Car et al conducted the cascade wind tunnel test[41]. In the preliminary wind tunnel tests, the secondary flow system failed to provide the required mass flow, momentum, and total pressure. The objective of this research is to first simulate the 3D flow field of the secondary flow system and identifies the problems that prevented the secondary flow system from delivering the proper jet conditions. Secondly, resolving the causes by redesigning the secondary flow system duct to achieve the required mass flow, momentum, and total pressure.

The wind tunnel test model was designed based on the 2D simulations done by Zha et al[38]. These 2D simulations used an inlet Mach number of 0.70 and a jet mass flow rate of 0.045 kg/s. During wind tunnel tests the inlet Mach number was reduced to M=0.3 because the secondary flow system could not provide the required mass flow rate. In an effort to discover the cause of the failure in the secondary flow system, the CFD models used in this paper match the experimental conditions at the inlet Mach number of 0.3. The next step of this research will be to study the case with the inlet Mach number of 0.7.

II. CFD Simulation of the Baseline Model

A. CFD Solver

The Fluent CFD software is used as the tool to simulate the cascade flows in this study. Fluent provides the capability to simulate the irregular geometry with unstructured grids. The k-epsilon turbulence model with wall function is used for all the simulations to save CPU time. The mean flow governing equations are the 3D compressible Navier-Stokes equations. Pressure based 2nd order upwind schemes are used to solve the governing equations.

B. CFD Setup of Baseline Model

The geometry of the blade and 3D duct system used in preliminary wind tunnel tests was utilized to establish a mesh for the CFD solver as shown in isometric in Figure 1 and a blowup side view in Figure 2. The suction surface turns 70 degree to axial. The chord length is 5.17", the pitch is 2.976", and the solidity of the cascades is 1.737. The design intent is to turn the incoming flow with 68 degree flow angle to axial with an inlet Mach number of 0.7. The spanwise length is 6". The bottom and top wind tunnel walls are simulated in the CFD model.

The injection duct, suction duct, and main flow passage were meshed using the Cooper meshing scheme in Gambit, and is illustrated in Figure 1. The inlet boundary is located one chord length upstream of the blade leading edge and the exit boundary is located two chord lengths downstream of the blade trailing edge. The total cell count for the main flow region along with the ducts is 553,244 cells. A view looking at the bottom tunnel wall where the ducts pass through is shown in Figures 2. A 10 node boundary layer was applied to the airfoil, a 16 node boundary layer was applied to the top and bottom tunnel walls, and there are totally 13 points across the jet slot, 50 grid points in the spanwise direction with the mesh clustered near the two wind tunnel walls. The total grid points on one side of the cascade blade (suction or pressure) is 150, among them 70 are in the jet slot in the streamwise direction. The averaged Y plus value is about 20.

The cascade inlet boundary condition has the total pressure of 14.2 psi, a total temperature of 280.37 K, and a flow direction of 68˚, which are all from the experiment. The outlet boundary condition has the static pressure iterated to match the experimental cascade inlet Mach number 0.3.

The injection duct inlet total pressure and total temperature are from the experiment and the values

Final Simulation Parameters		
Cascade Inlet	Value	Wind Tunnel Test Variable
Total Pressure	14.2 psi	31 - Tunnel Total Pressure
Total Temperature	280.37 K	36 - Tunnel Total Temperature
Flow direction at 68˚ to the inlet boundary		
Cascade Outlet	Value	
Static Pressure	13.8 psi	
Injection Duct Inlet	Value	Wind Tunnel Test Variable
Total Pressure	16.5 psi	results from wind tunnel tests
Total Temperature	312.45 K	from wind tunnel tests
Suction duct Outlet	Value	
Static Pressure	9.65 psi	results from individual duct simulation

Table 1. Final Simulation Parameters.

are given in Table 1. The suction duct exit static pressure is iterated to match the cascade inlet Mach number and the mass flow rate of the inject jet. The final values are given in Table 1. These values gave an inlet mach number of 0.31, an injection mass flow rate of 0.0227 kg/s, and a suction mass flow rate of 0.0225 kg/s.

C. Flow Field Results of CFD Wind Tunnel Model

Streamlines on the suction surface of the airfoil are illustrated in Figure 3, where the flow is moving from left (inlet) to right (outlet), the area of separation is seen as a region of recirculating flow near the top wall. A view of the streamlines over the pressure surface is shown in Figure 4, where the flow is moving from left (inlet) to right (outlet), and also shows this region of separating low momentum flow near the top wall.

To see how the jet interacts with the main flow, streamlines were released from the inlet of the injection duct and are illustrated in Figure 5, again the flow in this figure is moving from left (inlet) to right (outlet), and Figure 6 (looking into the domain from the cascade inlet, downstream). It is quite visible in these views how the flow leaving the injection duct has a large transverse velocity component and is not aligned with the main cascade flow for a large section of the suction surface, mainly from the bottom wall to well past the mid-span. A quantitative value of this transverse velocity direction in the injection slot is the average z-velocity (spanwise velocity); in this case the average z-velocity in the injection slot is -204.6 ft/s. Ideally the average z-velocity would be 0 ft/s, this would mean the jet flow is completely aligned with the main flow. Figure 7 is a plot of the z-velocity distribution of the injection jet in the spanwise direction, the position is from 0 (the top wall) to 6 (the bottom wall). This z-velocity distribution shows a very high negative z-velocity near the bottom wall, this is due to the fact that the injection jet simply bleeds straight through from the duct and has been turned very little.

Figure 8 illustrates the streamlines in the injection duct only. In Figure 8 one can see that the flow is not turning well near the inlet of the duct. There is a large low momentum area near the closed end of the duct at the top wall and is seen as a re-circulating region of flow in Figure 8; this region causes large losses, which weakens the jet near the top wall and causes the cascade flow to separate near the top wall. Figure 9 is the velocity vector field at the mid-span plane which shows that the jet is tangent to the blade surface and the main flow is attached in that region.

D. 1D Analysis

To determine the maximum amount of mass flow the baseline design ducts could pass under choked conditions, a 1D analysis was conducted using Eq. (1)[42], under choked conditions where M=1.

$$\dot{m}^* = P_0 A^* \left(\frac{\gamma}{RT_0} \right)^{1/2} \left(\frac{2}{\gamma + 1} \right)^{(\gamma+1)/2(\gamma-1)} \tag{1}$$

For the injection duct the smallest area the flow must pass through is the throat near the injection slot, A*= 0.2143 in^2. Using the injection parameters from Table 1 the maximum mass flow rate is $\dot{m}^* = 0.03597$ kg/s. For the suction duct the smallest area the flow must pass through is also at the throat near the suction slot, A*= 0.26713777 in^2. Using the suction parameters found in the CFD simulation the maximum suction mass flow rate is $\dot{m}^* = 0.0349$ kg/s. This 1D analysis shows that the originally designed ducts have enough area to pass the mass flow rate required at low freestream mach numbers, $\dot{m}^* = 0.0227$ kg/s, but does not have the available area to pass the expected mass flow rate needed at higher freestream mach numbers, $\dot{m}^* = 0.045$ kg/s, this is the reason why the wind tunnel model did not perform at the desired inlet Mach number of M=0.7.

III. CFD Simulated 9-Port Injection Duct Model

A. Geometry and Mesh of 9-Port Injection Duct Model

To align the co-flow jet with the main flow direction, the injection duct is partitioned into multiple ports (ducts). First, a 5-port model was simulated but proved to be less effective than the baseline model. Figure 10 shows the main cascade flow for the 5-port simulation. The 5-port simulation actually had a jet with a large positive z-velocity near the top and bottom wall and it was this result which led to the addition of fins to the 9-port models. The 9-port internal duct used in the final simulation is illustrated in Figure 11 and a blowup of the outlet area with the added fins is illustrated in Figure 12. The added fins shown in Figure 12 were designed to help straighten the flow just prior to the flow exiting through the injection slot. The same meshing scheme and boundary layers were applied to

the 9-port duct as was used in the previous simulations but again due to the added structure of more internal ducts the total cell count increased to 1,110,836 cells.

Table 3 shows the inlet areas of the 9 ports as well as their area ratios when compared to the first port, while all of the exit areas are equal. In this 9-port duct simulation the inlet areas were designed to be larger near the top and bottom walls so that the jet would be more energetic and may help to alleviate the separation due to wall effects. Port 9 (near the top wall) was designed to have the largest inlet area because past simulations have shown the top wall to be the region suffering the most pressure loss. A side view of the 9-port internal duct blade, shown in Figure 13, has been added to help demonstrate the arrangement and orientation of the ports.

	Area (in^2)	Area Ratio to 1st port
Inlet 1	0.02422	
Inlet 2	0.01996	82%
Inlet 3	0.02122	88%
Inlet 4	0.02099	87%
Inlet 5	0.02054	85%
Inlet 6	0.02260	93%
Inlet 7	0.02135	88%
Inlet 8	0.02116	87%
Inlet 9	0.02646	109%

Table 3. 9-Port Duct

When the 9-port jet demonstrated a more uniform jet, the injection mass flow rate was increased to help attach the flow. The final boundary conditions for the 9-port internal duct blade are listed in Table 4. These values gave a cascade inlet mach number of 0.34, an injection mass flow rate of 0.047kg/s, and a suction mass flow rate of 0.033 kg/s. The suction duct was very close to choking over most of the duct exit plane and therefore the mass flow rate was not able to match the injection mass flow rate. As visible in Figure 13 the suction duct has room to expand. The future designs will expand the suction outlet area to pass the desired mass flow rate.

Final Simulation Parameters		
Cascade Inlet	Value	Wind Tunnel Test Variable
Total Pressure	14.2 psi	31 - Tunnel Total Pressure
Total Temperature	280.37 K	36 - Tunnel Total Temperature
Flow direction at 68° to the inlet boundary		
Cascade Outlet	Value	
Static Pressure	13.8 psi	
Injection Duct Inlets	Value	
Total Pressure	30 psi	results from individual duct simulation
Total Temperature	312.45 K	results from individual duct simulation
Suction duct Outlet	Value	
Static Pressure	6 psi	results from individual duct simulation

Table 4. Final 9-Port Simulation Parameters.

B. Flow Field Results of 9-Port Injection Duct Model

Streamlines on the suction surface of the 9-port airfoil are illustrated in Figure 14, where the flow is moving from left (inlet) to right (outlet), the area of separation is shown as a small region of recirculating flow near the top wall, which is significantly smaller than the baseline geometry. Figure 15 is a plot of the z-velocity distribution of the injection jet in the spanwise direction, the position is from 0 (the top wall) to 6 (the bottom wall). This z-velocity distribution shows a jet which still has large Z velocities in both positive and negative directions but averages to 24.5 ft/s across the jet, which is much more uniform than in previous cases. This is evident in the streamlines being attached for most of the blade surface.

To see how the jet interacts with the main flow, streamlines were released from the inlet of the injection duct and are illustrated in Figure 16 (looking into the domain from the cascade inlet, downstream). From these streamlines it is quite visible that the jet flow released from the injection slot is nearly uniformly aligned to the main flow of the cascade. However, the jet near the top wall is still not as strong or uniform enough to achieve attached flow across the entire span of the blade.

Figure 17 shows streamlines within the 9-port injection duct. The flow within the ducts has recirculating flow near the high turning areas. It is these regions which squeeze the flow into smaller internal jets and gives the jet its positive and negative z-velocity distribution. The region of recirculating flow which most harmfully affects the uniformity of the jet is in the ports nearest to the top wall (ports 7, 8, and 9). Figure 18 is the velocity vector field at the mid-span plane which shows that the jet, as well as the main flow, is attached in this region, which correlates directly to the results seen in the streamlines.

C. 1D Analysis

For the injection duct the smallest area the flow must pass through is at the duct inlet, A*= 0.19849 in^2. Using the injection parameters from Table 4 the maximum mass flow rate is $\dot{m}^* = 0.0633\ kg/s$. For the suction duct the smallest area the flow must pass through is located at the duct exit plane, A*= 0.3291 in^2. Using the suction parameters of P=11.73 psi the maximum mass flow rate is $\dot{m}^* = 0.041\ kg/s$. Due to the area being too small to pass the higher mass flow rate the suction duct was choking across most of its outlet. As mentioned the area for the outlet of the suction duct has more room to be expanded, as can be seen in Figure 13, and future simulations will be conducted with this expanded exit duct.

D. Overall Performance of the Three Secondary Flow Ducts

Performance data such as jet momentum coefficient, C_μ, for all models simulated in this report are displayed in Table 5. For all three cases the free stream velocities are fairly close and vary slightly due to different levels of

blockage caused by separation on the blades. C_μ was increased in the 9-port case because the injection jet was observed to be more uniform at the higher mass flow rate. The raising of the C_μ resulted in the flow becoming attached for nearly the entire chord length.

To examine the diffusion factor, DF, of each designed geometry, the diffusion factor is defined in Eq. (2). In Eq. (2) V_1 and V_2 is the velocity magnitude of the blade inlet and outlet, $V_{\theta 1}$ and $V_{\theta 2}$ is the tangential velocity at the blade inlet and outlet, and σ is the solidity defined as the chord divided by the pitch.

$$DF = 1 - \frac{V_2}{V_1} + \frac{V_{\theta 1} - V_{\theta 2}}{2\sigma V_1} \tag{2}$$

The DF for all three blades are displayed in Table 5. As expected the DF for the 9-port model is greater than that of the baseline and 5-port models. Even though the baseline geometry has a diffusion factor of 0.7 the flow field is much less uniform than the 9-port model and the solution can not be used to study the 2D cascade performance. The DF at the midpsan shows the severity of the non-uniform flow.

All Values are in SI units	Jet Velocity	Injection Mass flow	$\rho\infty$	$U\infty$	S	C_μ	DF	DF at Midspan
Wind Tunnel Model	166.13	0.02256	1.16	101.71	0.0376	0.0166	0.70	0.75
5-port Model	134.39	0.02168	1.18	95.84	0.0376	0.0143	0.62	0.68
9-port Model	254.80	0.04737	1.15	113.14	0.0376	0.0437	0.74	0.78

Table 5. Blade Performance Data.

Figures 19, 20, and 21 depict the isentropic Mach number distribution over the surface of the blades at the midpsan, 20%, and 80% of the span for the baseline, 5-port, and 9-port models, respectively. The 9-port model shows a much higher blade loading with a peak Mach number of 0.42 on the suction surface when compared to the 0.36 and 0.34 of the baseline and 5-port models, respectively. Also, the 9-port model shows much larger loading over all three span locations, indicating a more uniform flow over the span of the blade then either the baseline or 5-port models. Again this higher loading can be seen by a direct comparison of the isentropic Mach numbers at the midpsan location, as illustrated in Figure 22.

IV. Work in Progress

To match the desired inlet mach number of 0.7, in wind tunnel testing, further design work will be done with other 9-port ducts in order to achieve better uniformity and a jet which stays completely attached. This will be done by changing the size of the inlets for each port, adjusting the curvature within the ducts, and increasing the suction duct to allow the appropriate mass flow rate.

V. Conclusion

This research presents several 3D CFD designs of the secondary flow system for a co-flow jet cascade previously wind tunnel tested by AFRL. The simulations found large areas of separation over much of the span. The baseline geometry has large transverse velocity components and the flow is very non-uniform. This transverse velocity component was reduced by dividing the internal duct into 9 separate ports. This 9-port design proved to turn the injection jet flow more effectively and gave a more uniform jet across the entire slot, resulting in a DF=0.74 while using a C_μ=0.0437. Design changes are currently under way to improve the uniformity of the jet in order to achieve the desired inlet Mach number of 0.7.

Acknowledgments

The authors would like to thank AFRL/CARL for their funding support to conduct this research.

References

1. A. Wadia, P. Szucs, and D. Crall, “Inner Workings of Aerodynamic Sweep ," ASME Journal of Turbomachinery, vol. 120, pp. 671{682, 1998.
2. A. Wadia, P. Szucs, and D. Crall, “Forward Swept Rotor Studies in Multistage Fans with Inlet Distortion." ASME 2002-GT-30326, 2002. 10

3. S. Gallimore, J. Bolger, and N. Cumpsty, “The Use of Sweep and Dihedral in Multi-stage Axial Flow Compressor Blading, Part II: Low and High Speed Design and Test Verication." ASME Paper GT-2002-30328, 30329, June 3-6, 2002.
4. J. A. Brent and D. R. Clemmons, “Single-Stage Experimental Evaluation of Tandem-Airfoil Rotor and Stator Blading for Compressors, Part 8." NASA-CR-134713, Nov. 1974.
5. J. A. Brent, J. G. Cheatham, and A. W. Nilsen, “Single-Stage Experimental Evaluation of Tandem-Airfoil Rotor and Stator Blading for Compressors, Part 1 Analysis and Design of Stages A, B, and C. ." NASA-CR-120803, June 1972.
6. M. Hathaway, “Self-Recirculating Casing Treatment Concept for Enhanced Compressor Performance." ASME 2002-GT-30368, 2002.
7. Q. Yu, Q. Li, and L. L, “Experimental Researches on Improving Operating Stability of A Single Stage Transonic Fan." ASME 2002-GT-30640, 2002.
8. D. Rabe and C. Hah, “Application of Casing Circumferential Grooves for Improved Stall Margin in a Transonic Axial Compressor." ASME 2002-GT-30641, 2002.
9. M. Gad-el Hak, “Flow Control: The Future ," Journal of Aircraft, vol. 38, pp. 402{418, 2001.
10. M. Gad-el Hak, Flow Control, Passive, Active, and Reactive Flow Management. Cambridge University Press, 2000.
11. V. Modi, M. Fernando, and T. Yokomizo, “Drag Reduction of Blu Bodies Through Moving Surface Boundary Layer Control." AIAA Paper No. 90-0298, 1990.
12. D. Cichy, J. Harris, and J. MacKay, “Flight Tests of a Rotating Cylinder Flap on a North American Rockwell YOV-10A Aircraft." NASA CR-2135, 1972.
13. L. C. Bradley, “An Experimental Investigation of A Sting-Mounted Finite Circulation Control Wing." M.S. Thesis, Air Force Institute of Technology, 1995.
14. N. Wood, L. Robert, and Z. Celik, “Control of Asymmetric Vortical Flows over Delta Wings at High Angle of Attack," Journal of Aircraft, vol. 27, pp. 429{435, 1990.
15. N. Wood and L. Robert, “Control of Vortical Lift on Delta Wings by Tangential Leading-Edge Blowing," Journal of Aircraft, vol. 25, pp. 236{243, 1988.
16. N. Wood and J. Nielsen, “Circulation Control Airfoils-Past, Present, Future." AIAA Paper 85-0204, 1985.
17. R. J. Englar, L. A. Trobaugh, and R. Hemmersly, “STOL Potential of the Circulation Control Wing for High-Performance Aircraft," Journal of Aircraft, vol. 14, pp. 175,181, 1978.
18. R. J. Englar, “Circulation Control for High Lift and Drag Generation on STOL Aircraft," Journal of Aircraft, vol. 12, pp. 457{463, 1975.
19. A. Smith, “High-Lift Aerodynamics," Journal of Aircraft, vol. 12, pp. 501{530, 1975.
20. J. Lin, S. Robinson, R. McGhee, and W. Valarezo, “Separation Control on High Reynolds Number Multi-Element Airfoils." AIAA Paper 92-2636, 1992.
21. K. McManus and J. Magill, “Airfoil Performance Enhancement Using Pulsed Jet Separation Control." AIAA Paper 97-1971, 1997.
22. K. McManus and J. Magill, “Separation Control in Incompressible and Compressible Flows Using Pulsed Jets." AIAA Paper 96-1948, 1996.
23. H. Johari and K. McManus, “Visulation of Pulsed Vortex Generator Jets for Active Control of Boundary Layer Separation." AIAA Paper 97-2021, 1997.
24. J. Paduano, A. Epstein, L. Valavani, J. Longley, and E. Greitzer, “Active Control of Rotating Stall in a Low Speed Axial Compressor," ASME Journal of Turbomachinery, vol. 115, pp. 48{56, 1993.
25. J. Haynes, G. Hendricks, and A. Epstein, “Active Stabilization of Rotating Stall in a Three-Stage Axial Compressor ," ASME Journal of Turbomachinery, vol. 116, pp. 226-239, 1994.
26. D. Gysling and E. Greitzer, “Dynamic Control of Rotating Stall in Axial Flow Compressors Using Aeromechanical Feedback ." ASME Paper 94-GT-292, 1994.
27. I. J. Day, “Active Suppression of Rotating Stall and Surge in Axial Compressors," ASME Journal of Turbomachinery, vol. 115, pp. 40{47, 1993.
28. H. Weigl, J. Paduano, L. Frechette, A. Epstein, E. Greitzer, M. Bright, and A. Strasizar, “Active Stabilization of Rotating Stall and Surge in a Transonic Single-Stage Axial Compressor," Journal of Turbomachinery, vol. 120, pp. 625{636, 1998.
29. Z. Spakovszky, H. Weigl, J. Paduano, C. Van Schalkywk, K. Suder, and M. Bright, “Rotating Stall Controll in a High-Speed Stage with Inlet Distortion: Part I- Radial Distortion ," Journal of Turbomachinery, vol. 121, pp. 510{516, 1999.

30. Z. Spakovszky, C. Van Schalkywk, H. Weigl, J. Paduano, K. Suder, and M. Bright, “Rotating Stall Controll in a High-Speed Stage with Inlet Distortion: Part II - Circumferential Distiontion," Journal of Turbomachinery, vol. 121, pp. 517-524, 1999.
31. J. Kerrebrock, D. Reijnen, W. Ziminsky, and L. Smilg, “Aspirated Compressors.", ASME 97-GT-525, 1997.
32. A. Merchant, “Aerodynamic Design and Performance of Aspirated Airfoils." ASME 2002-GT-30369, 2002.
33. B. Schuler, J. L. Kerrebrock, and A. Merchant, “Experimental Investigation of an Aspirated Fan." ASME Paper 2002-GT-30370, June 3-6,2002.
34. B. Schuler, J. L. Kerrebrock, A. Merchant, M. Drela, and J. Adamczyk, “Design, Analysis, Fabrication and Test of an Aspirated Fan Stage." ASME Paper 2000-GT-618, May 8-11, 2000.
35. A. Merchant, M. Drela, J. L. Kerrebrock, J. Adamczyk, and M. Celestina, “Aerodynamic Design and Analysis of a High Pressure Ratio Aspirated Compressor Stage." ASME Paper 2000-GT-619, May 8-11, 2000.
36. N. Cumpsty, Compressor Aerodynamics. Longman Scientific & Technical, 1989.
37. W. Copenhaver, P. Koch, D. Car, W. Ng, S. Guillot, J. Estevadeordal, and C. Carter, “Improvement of a Counter-Swirl Stator Section with Ejector Pump Based Boundary Layer Control." Submitted for publication to ASME Journal of Fluids Engineering.
38. G.-C. Zha, (team members: David Car, and W. Copenhaver), “Super Diffusion Cascades Using Co-Flow Jet Flow Control." National Research Council Summer Faculty Final Report, Aug. 23, 2002.
39. R. Neuendorf and I. Wygnanski, “On a Turbulent Wall Jet Flowing over a Circular Cylinder," Journal of Fluid Mechanics, vol. 381, pp. 1-25, 1999.
40. G. Zha and C. Paxton, “A Novel Airfoil Circulation Augment Flow Control Method Using Co-Flow Jet." AIAA Paper 2004-2208, 2nd AIAA Flow Control Conference, June 28-July 1, 2004, Portland, Oregon.
41. Car, D., Kuprowicz, N. J., Estevadeordal, J., Zha, G.-C. and Copenhaver, W." Stator Diffusion Enhancement Using a Re-Circulating Co-Flowing Steady Jet" , ASME Paper GT2004_53086, ASME TURBO EXPO 2004, June 14-17, 2004, Vienna, Austria
42. M. J. Zucrow and J. D. Hoffman, *Gas Dynamics Volume 1*.John Wiley & Sons, pp. 146, 1976.

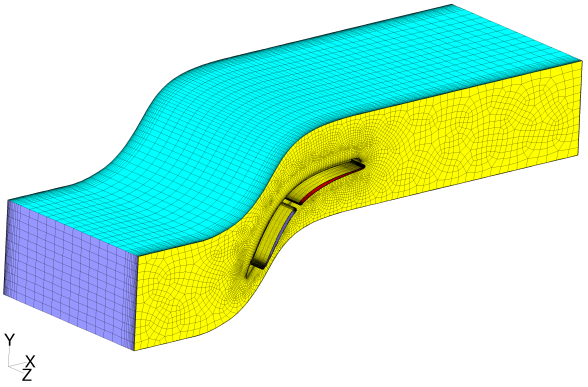

Figure 1: Cascade mesh and zones.

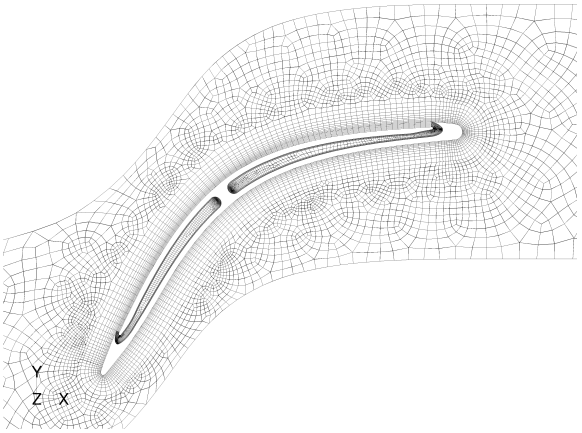

Figure 2: Cascade mesh side view, airfoil region.

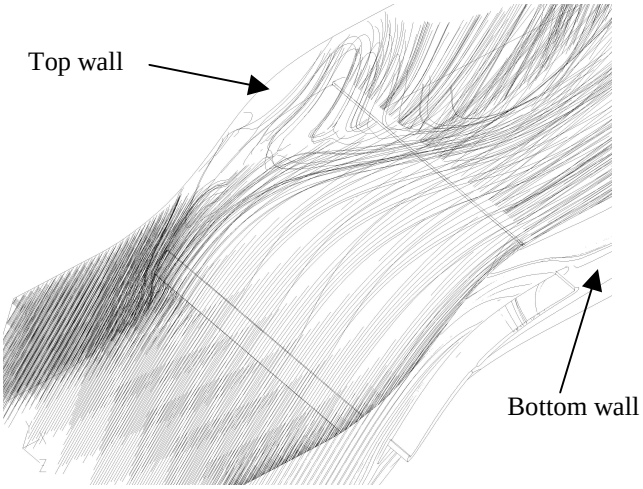

Figure 3: Streamlines over the suction surface (flow from left to right).

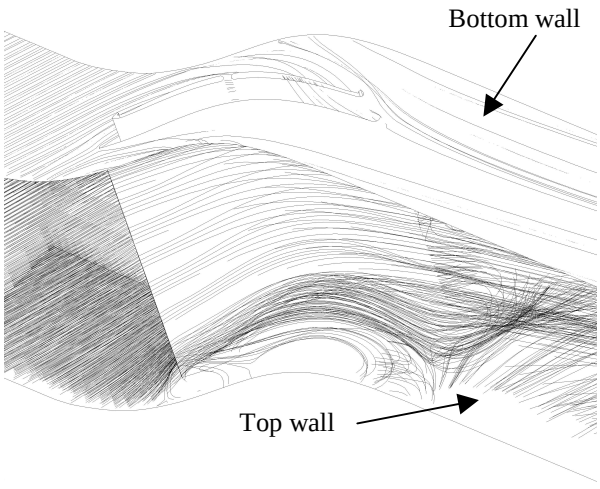

Figure 4: Streamlines over the pressure surface (flow from left to right).

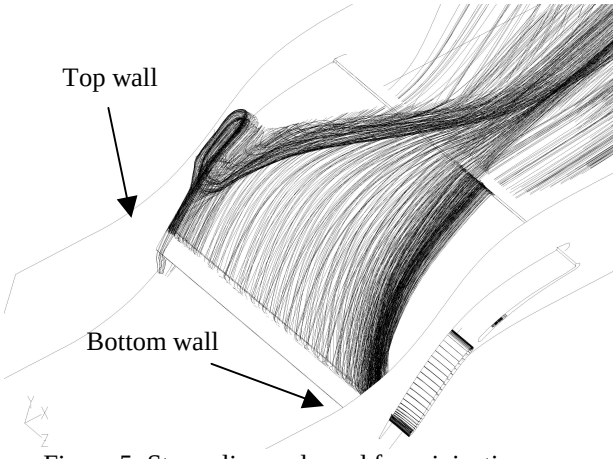

Figure 5: Streamlines released from injection inlet, view of the suction surface (main cascade flow from left to right).

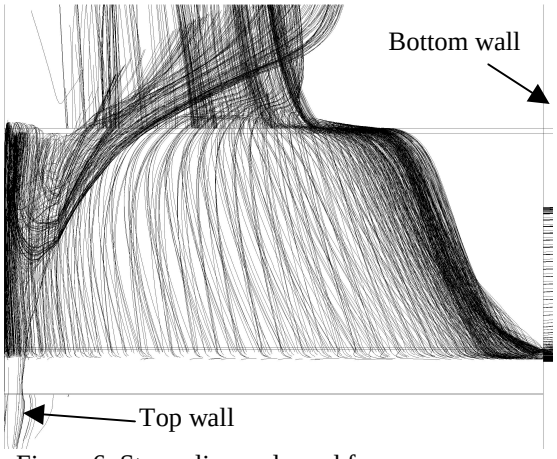

Figure 6: Streamlines released from injection inlet (view at cascade inlet downstream).

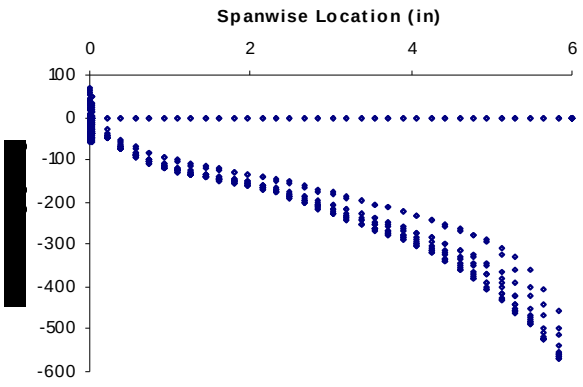

Figure 7: Z-velocity distribution spanwise across inject slot.

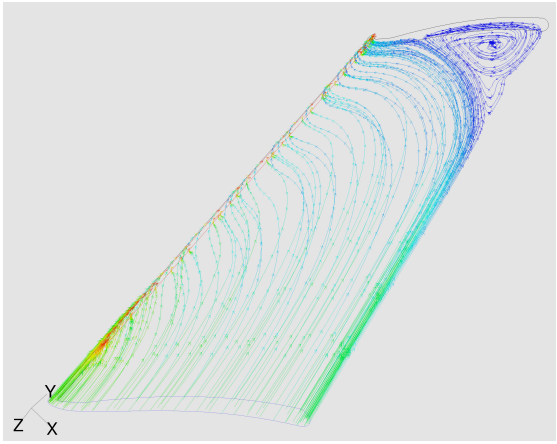

Figure 8: Mach streamlines, wall function treatment.

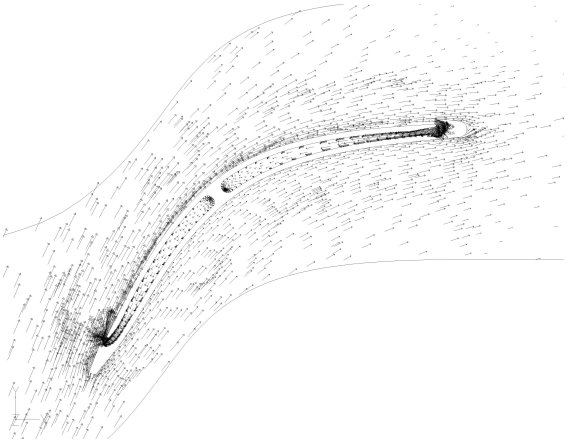

Figure 9: Cascade vectors around the airfoil at mid-span.

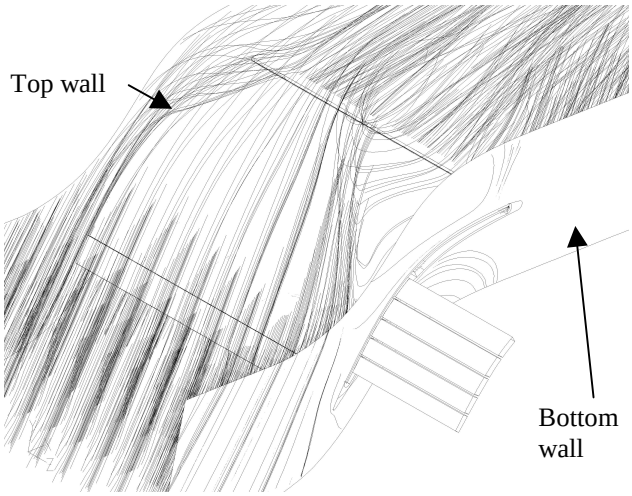

Figure 10: 5-Port duct streamlines over the suction surface (flow from left to right).

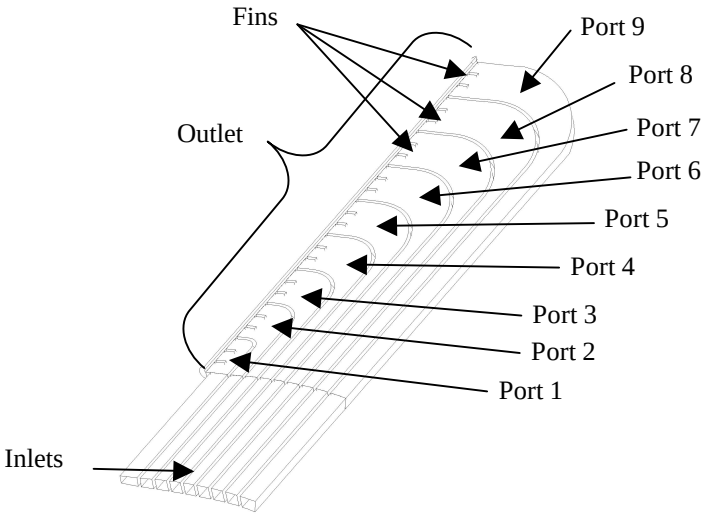

Figure 11: 9-Port Internal Duct structure.

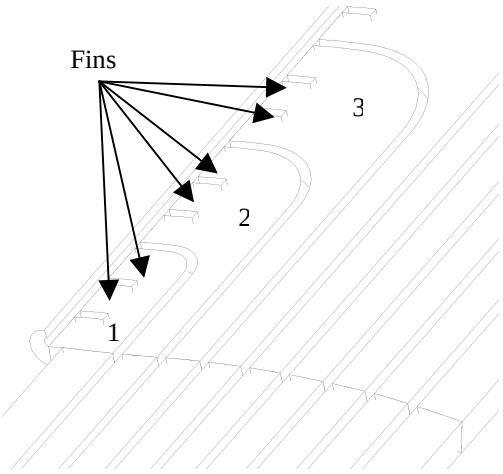

Figure 12: 9-Port Internal Duct Blowup of Outlet and Fin Area.

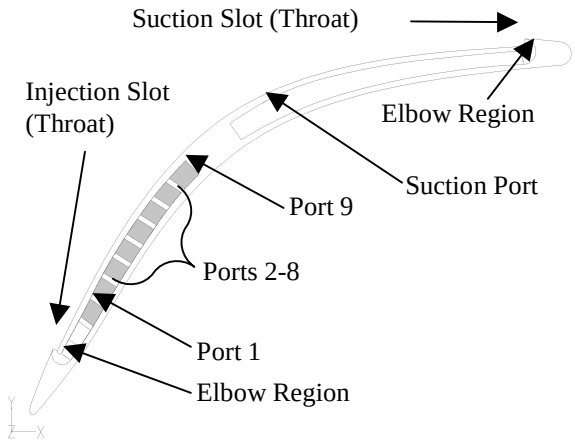

Figure 13: 9-Port Port internal duct blade side view.

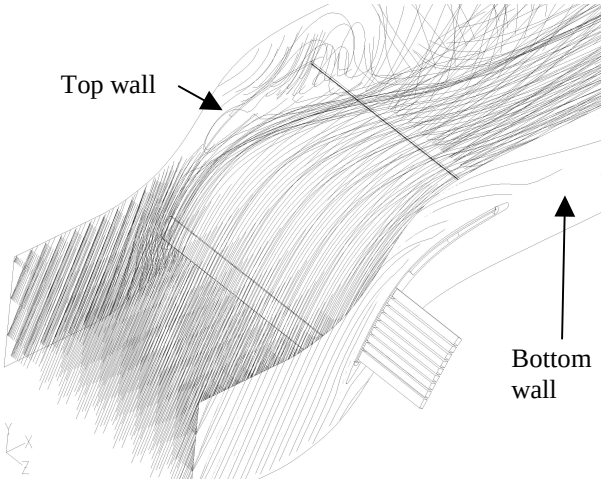

Figure 14: 9-Port duct streamlines over the suction surface (flow from left to right).

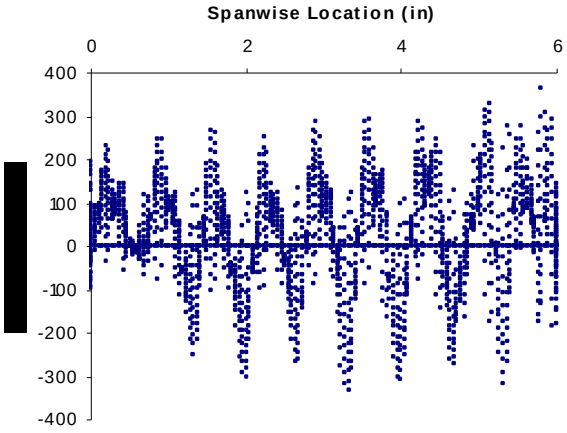

Figure 15: 9-Port Z-Velocity distribution spanwise across the injection slot.

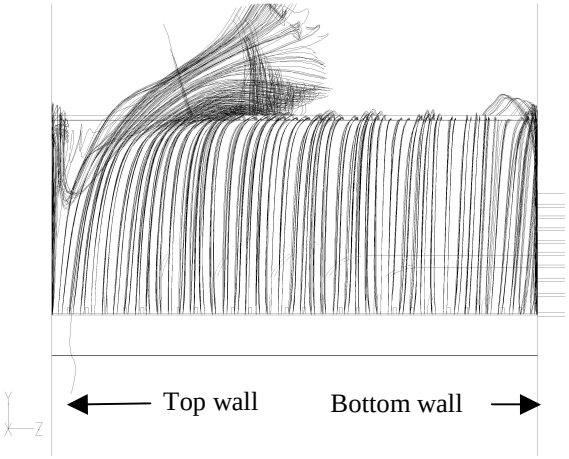

Figure 16: 9-port duct streamlines released from injection inlet (view at cascade inlet downstream).

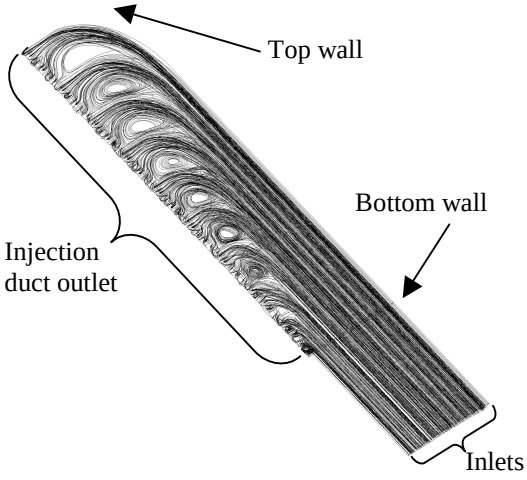

Figure 17: 9-port internal duct streamlines released from injection inlet.

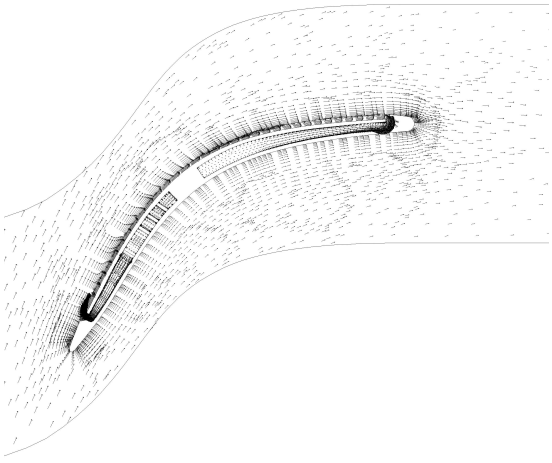

Figure 18: 9-port internal duct vectors around the airfoil at mid-span.

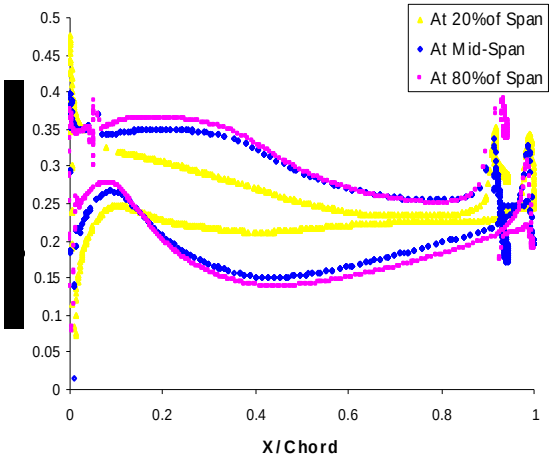

Figure 19: Wind Tunnel Model Isentropic Mach Distribution at midspan, 20% and 80% of span.

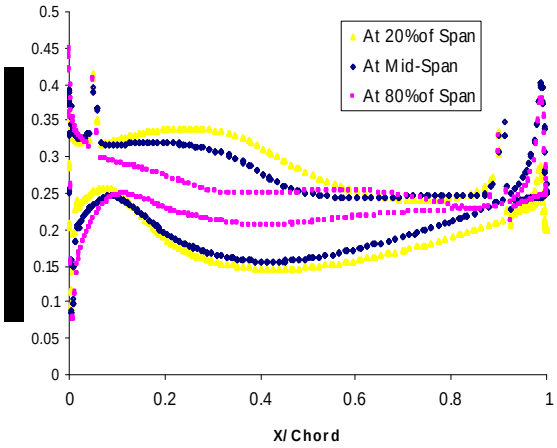

Figure 20: 5-Port Model Isentropic Mach Distribution at midspan, 20% and 80% of span.

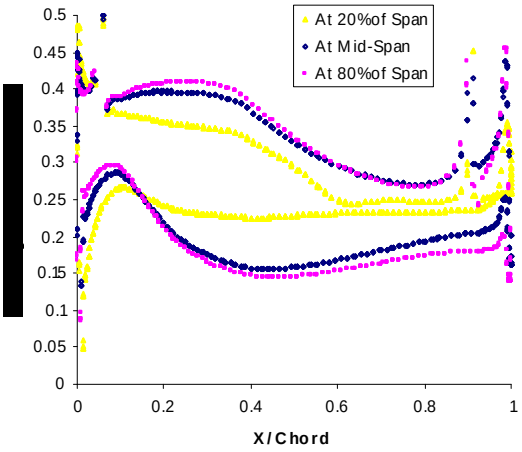

Figure 21: 9-Port Model Isentropic Mach Distribution at midspan, 20%, and 80% of span.

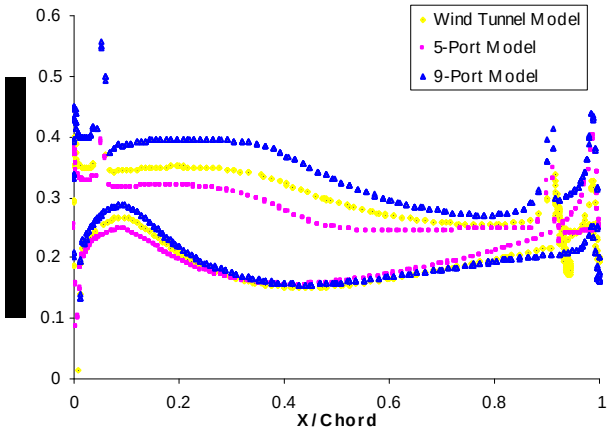

Figure 22: All Models Isentropic Mach Distribution at midspan.